Spatially precise light-activated dedoping in wafer-scale MoS_2 films

Debjit Ghoshal[1], Goutam Paul[1], Srikrishna Sagar[1], Cole Shank[1], Lauren Hurley[2,3], Nina Hooper[1], Jeiwan Tan[1], Kory Burns[4], Jordan A. Hachtel[5], Andrew J. Ferguson[1], Jeffrey L. Blackburn[1], Jao van de Lagemaat[1,2*], and Elisa M. Miller[1,2*]

[1]Materials, Chemistry, and Computational Sciences Directorate, National Renewable Energy Laboratory; Golden, Colorado, 80401, USA.
[2]Renewable & Sustainable Energy Institute (RASEI), Boulder, Colorado, 80303, USA.
[3]Electrical, Computer and Energy Engineering, University of Colorado Boulder, Boulder, Colorado, 80309, USA.
[4]Department of Materials Science and Engineering, University of Virginia, Charlottesville, Virginia, 22904, USA.
[5]Center for Nanophase Materials Sciences, Oak Ridge National Laboratory, Oak Ridge, Tennessee, 37830, USA.

**Correspondence to be addressed to jao.vandelagemaat@nrel.gov and elisa.miller@nrel.gov*

2D materials, particularly transition metal dichalcogenides (TMDCs), have shown great potential for microelectronics and optoelectronics. However, a major challenge in commercializing these materials is the inability to effectively dope them at a wafer scale with high spatial fidelity. We use interface chemistry with the underlying substrate oxide and concomitant exposure to visible light in ambient conditions for photo-dedoping wafer scale MoS_2. We hypothesize that the oxide layer traps photoexcited holes, leaving behind long-lived electrons that become available for surface reactions with ambient air at sulfur vacancies resulting in dedoping. Additionally, we showcase high fidelity spatial control over the dedoping process, by laser writing, and fine control over the degree of doping by modulating the illumination time and power density. This localized change in MoS_2 doping density is very stable (at least 7 days) and robust to processing conditions like high temperature and vacuum. The scalability and ease of implementation of this approach can address one of the major issues preventing the "Lab to Fab" transition of 2D materials and facilitate its seamless integration for commercial applications in multi-logic devices, inverters, and other optoelectronic devices.

Atomically thin semiconductors have shown a lot of promise for next generation microelectronics due to their thinness, unique layer-dependent band structure, and exceptional optoelectronic properties[1,2]. These distinctive optical and electronic properties coupled with the ultrathin nature of layered materials have led to various applications in flexible electronics, gas sensing, and neuromorphic computing[3,4]. While earlier efforts focused on devices from exfoliated samples, more recently, chemical vapor deposition (CVD) and metal organic chemical vapor

deposition (MOCVD) techniques have led to large area wafer scale growth of monolayers of 2D materials[5–10]. This has enabled circuit scale demonstrations of field effect transistors (FETs) of the 2D monolayers for devices like ring oscillators, inverters, and logic operators[11,12].

Although extensive efforts have focused on wafer scale growth of 2D materials, very little has been done to develop techniques to tune their carrier density using commercially feasible approaches. Having the ability to differentially dope 2D materials n- or p-type at wafer scale could enable multi-valued logic gates (> 2 states) with substantially improved information density per unit area and reduced power consumption[13] over existing technology. The ability to dope these materials with high-spatial resolution forms the basis of many emerging optical and optoelectronic devices[14,15].

While doping in silicon can be easily accomplished by bombarding ions of the dopant material on the silicon wafer,[16] this technique cannot be readily extended to 2D materials that are damaged by the highly energetic ion beams of the dopant material[17]. Electrostatic gating has emerged as an effective way to control doping densities in 2D materials but this comes at the cost of extensive microfabrication and is limited to two states[18]. While multiple gates can in principle result in localized control of doping, this leads to drastic increase in complexity of fabrication and therefore cost[19,20].

More recently, efforts have focused on interfacial and chemical methods of doping graphene and transition metal dichalcogenides (TMDCs)[21,22]. While these devices were good proof of concept demonstrations, the samples were fabricated by mechanical exfoliation making it unfeasible for practical implementation. Similarly, native oxidation of few layer InSe, synthesized by mechanical exfoliation was used as a novel interface to boost charge trapping, resulting in doping of the unoxidized InSe channels[23]. However, this approach is less controllable and limited to unstable materials. Dynamic doping with light and applied potential has been demonstrated in few layer $MoTe_2$ but couldn't be extended to other TMDCs like MoS_2 and WS_2, which are less susceptible to defect formation and more stable under illumination/applied potential[24–26]. Chemical doping in solution-processed few layer MoS_2 thin films has resulted in area-selective doping but is often unstable to processing conditions[27]. Similarly, electron beam exposure as a doping method has complexity and cost considerations[28,29]. Substitutional doping has shown promise as a scalable

technique to dope large area TMDCs but this technique lacks spatial control making it less useful for fabrication of optoelectronic devices where such control is critical[30–32].

We were inspired by multiple reports demonstrating variability of the optoelectronic properties of monolayer TMDCs under ambient conditions[33,34]. Due to their ultrathin nature, the electronic and optical properties of TMDCs can be extremely sensitive to the environment they are placed in. While this makes benchmarking a challenge with these materials, it also offers opportunities to modulate their properties (including doping/dedoping) provided one can unravel the salient mechanism(s)[35–38]. Recent reports have shown large changes in photoluminescence (PL) of monolayer TMDCs upon exposure to light in ambient/controlled conditions[39–44]. Several studies, including ours, have linked this observation to the passivation of vacancy-related defect states through chemisorption and/or physisorption processes[45–49]. While the exact mechanism is still hotly debated, these results demonstrate the potential to photomodulate optoelectronic properties of TMDCs.

In this work, we demonstrate that the underlying oxide interface between the monolayer MoS_2 and the substrate plays a critical role in the observed enhancements in PL (under ambient conditions) upon illumination. We conclusively show with Kelvin Probe Force Microscopy (KPFM) measurements that these enhancements in PL upon illumination correlate directly to doping level changes. We leverage this idea to develop a facile approach to controllably dedope wafer scale MoS_2 with high spatial resolution that is stable for at least a week. Additionally, we show control over doping density, by tuning the time and power of illumination. This demonstration opens avenues for lithography-free fabrication of multi-logic devices in MoS_2 at wafer scale. We anticipate that the scalability and ease of implementation of this approach will open up avenues to develop wafer-scale 2D material circuitry hitherto unexplored.

Results

PL enhancement indicates de-doping of large-area monolayer MoS_2 upon illumination.

Wafer-scale 2H MoS_2 grown by CVD is used for this study (Fig. S1 and S2). Raman spectroscopy confirmed that the MoS_2 (Fig. 1a, photograph) is monolayer (~19 cm^{-1} separation between E_{2g} and A_{1g} modes) and in the 2H phase (Fig. 1b). Raman mapping confirms the homogeneity of the film (Fig. S3), and high-angle annular dark field scanning transmission

electron microscopy (HAADF-STEM, Fig. 1c) confirms the 2H MoS_2 phase and film quality. HAADF-STEM images (Fig. S4) show presence of atomic defects in the as grown film. In addition, the A and B exciton absorption positions at 1.87 eV and 2.02 eV (Fig. S5) further confirms monolayer MoS_2[30].

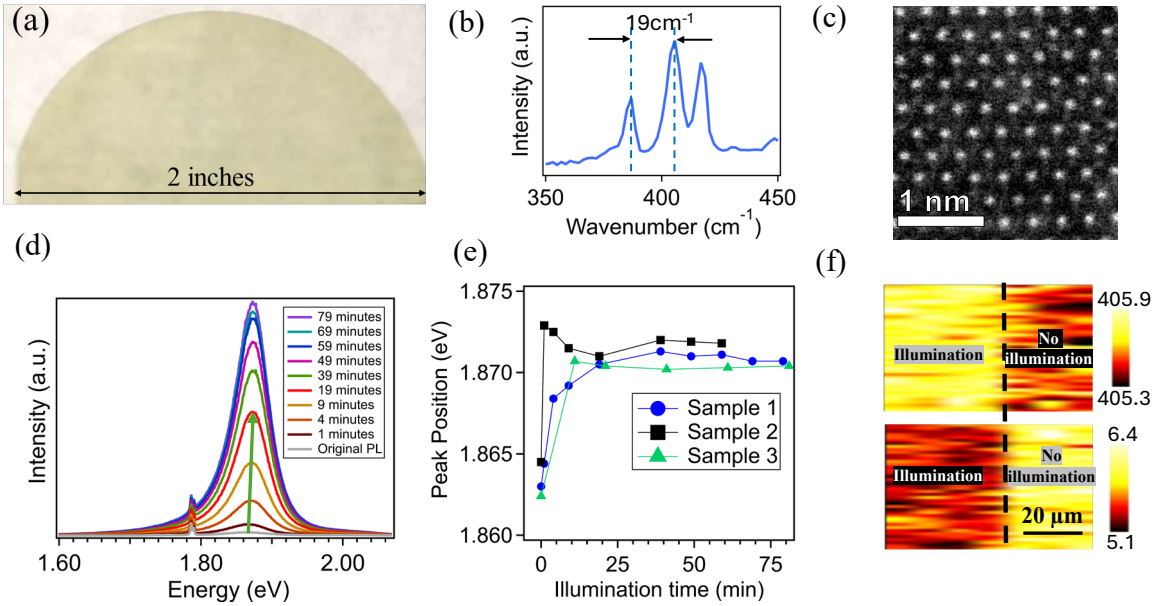

Fig. 1: Photode-doping effect in monolayer MoS_2. (a) Camera image of wafer scale MoS_2. (b) Raman splitting confirming MoS_2 with splitting between the E_{2g} and A_{1g} modes of 19 cm^{-1}. (c) HAADF-STEM image from monolayer MoS_2. (d) Photosoaking effect in MoS_2 showing increase in PL on illumination with 532 nm laser at a power density of 423.7 $\mu W/\mu m^2$. (e) Changes in peak position of monolayer MoS_2 as a function of illumination time. (f) Raman shift mapping data for the A_{1g} mode of MoS_2 showing changes in peak position (top panel) and peak width (bottom panel) with/without illumination to 532 nm laser. Units for both the color scales are cm^{-1}.

Interestingly, PL measurements on the MoS_2 films show changes in intensity and peak position upon illumination with a 532 nm laser under ambient conditions (Fig. 1d). While the PL is initially weak due to the n-type doping as grown[50,51], there is almost 80x enhancement upon illumination. The PL peak also blue shifts 100 meV for the initial 19 mins before stabilizing (Fig. 1d, sample 1). The absolute magnitudes of PL changes were sample dependent; however, the trends in PL intensity and peak position (Fig. 1e) were qualitatively similar for all samples. The blue shift and increased intensity in MoS_2 PL can be explained by spectral redistribution as the dominant PL character changes from charged exciton (trion) to neutral exciton emission. These

observations indicate a reduction in doping level upon illumination with 532 nm laser under ambient conditions. The integrated PL intensity for various illumination times is shown in Fig. S6a, where the PL changes show a saturation behavior and eventually plateau.

Significant PL enhancement was only seen for an illumination laser photon energy exceeding the MoS_2 bandgap (E_g = 1.87 eV; e.g., 532 nm (2.33 eV) and 633 nm (1.96 eV) lasers), while sub-bandgap illumination with 785 nm (1.58 eV) did not generate PL changes (Fig. S6b). Note that the illumination laser wavelength varies for these measurements (532, 633, or 785 nm), but the PL measurement is always performed with 532 nm excitation laser light.

Raman modes are used to determine changes in carrier concentration and strain in monolayer MoS_2, where the A_{1g} mode is more sensitive to carrier concentration (doping) and the E_{2g} mode is more sensitive to strain (and less sensitive to doping)[51,52]. Raman mapping (Fig. 1f and Fig. S7) confirmed differences in peak position and FWHM between the illuminated and unilluminated regions of the MoS_2 for the A_{1g} mode while the E_{2g} mode showed no significant change in either the peak position or FWHM. The A_{1g} mode shifted to higher energy and showed narrower FWHM on MoS_2 areas illuminated with the laser (where the PL is stronger and blue shifted) consistent with dedoping of MoS_2. The lack of change in the E_{2g} mode suggests the illumination affects only doping densities (and not strain)[51,52]. Trends from the Raman shifts as well as PL enhancements insinuate (and are consistent with) dedoping on illumination.

KPFM confirms that PL changes are related to photo-dedoping

By rastering a focused laser beam using the confocal Raman/PL setup, we produced well controlled photo-patterns (details in the Materials and Methods section) on the MoS_2 with high spatial fidelity that can be mapped with PL and Kelvin Probe Force Microscopy (KPFM) measurements to better understand the changes driving PL enhancements.

PL maps and corresponding surface potential images (measured on the same area) mirror each other, showing obvious anti-correlations between spatially dependent PL intensity and surface potential of the MoS_2 film (Fig. 2c and 2d). The areas of MoS_2 illuminated with the 532 nm laser (green stripes in Fig. 2a) showed a concomitant increase in PL (Fig. 2c) and decrease in surface potential (Fig 2d and 2f), both of which are consistent with the initially n-type MoS_2 Fermi level moving towards the middle of the bandgap (becoming more intrinsic).

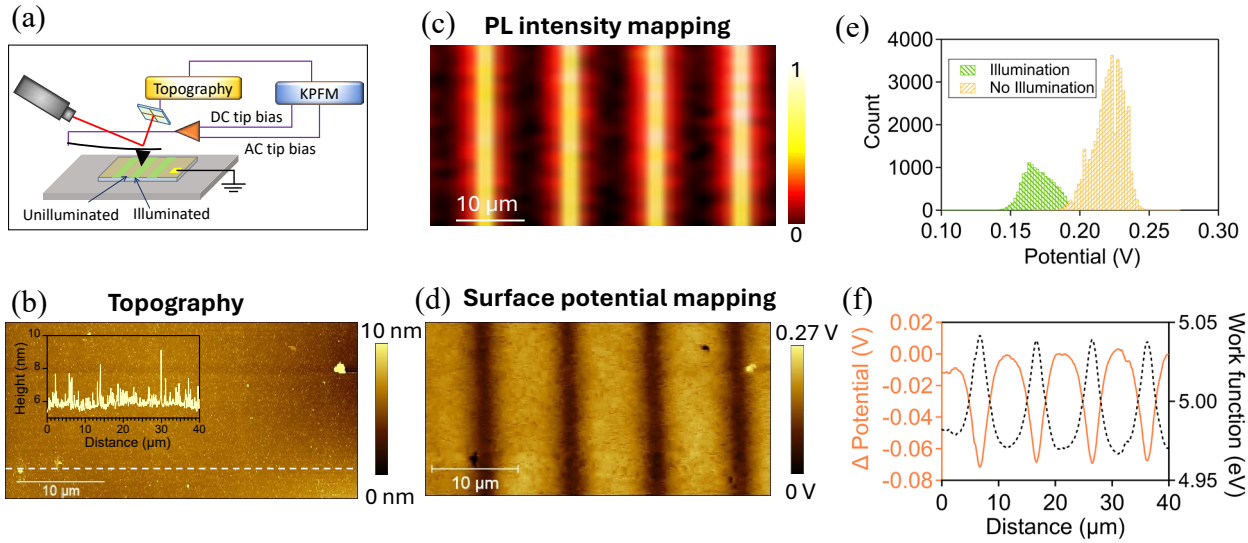

Fig. 2: KFPM measurements for confirmation of photo-dedoping upon illumination. (a) Schematic of the KPFM setup for mapping changes in surface potential between the illuminated and not illuminated parts. (b) AFM images confirm no significant changes in the topography the areas with and without illumination. (c) PL mapping data showing increments in PL at 1.87 eV upon illumination. PL intensity has been normalized to the pixel with the highest intensity. (d) KPFM data is anti-correlated with the PL, illustrating decreased surface potential with increased PL. (e) Distribution of surface potential for illuminated and not illuminated parts. (f) Variation of surface potential and work function as a function of position.

Analysis of the KPFM images reveals a distribution of measurements with different potentials centered around ~170 mV and ~230 mV for areas that were and were not exposed to illumination (Fig. 2e). AFM height scans (Fig. 2b) confirmed no topographic changes within the sensitivity limits of 0.5 nm. Additionally, Raman E_{2g} measurements confirmed no structural changes post illumination. Therefore, the increase in PL and work function can be directly attributed to photo-dedoping with the MoS_2 becoming more intrinsic and the PL more excitonic in nature. The ability to change doping levels in monolayer MoS_2 upon illumination offers distinctive capabilities for spatial control over carrier densities by selectively exposing chosen regions to light.

Fine control of doping density

We further investigated the role of the illumination conditions to elicit better control over photo-dedoping in large area monolayer MoS_2. KPFM (Fig. 3a) and PL (Fig. 3b) mapping show changes in surface potential and emission intensity with different illumination times between 1 and 30 secs at fixed power density. Longer illumination times produce larger shifts in surface potential and more intense PL emission. The illumination time dependence of surface potential and PL are strongly correlated, as shown in the line scans of Fig.3c and 3d, respectively.

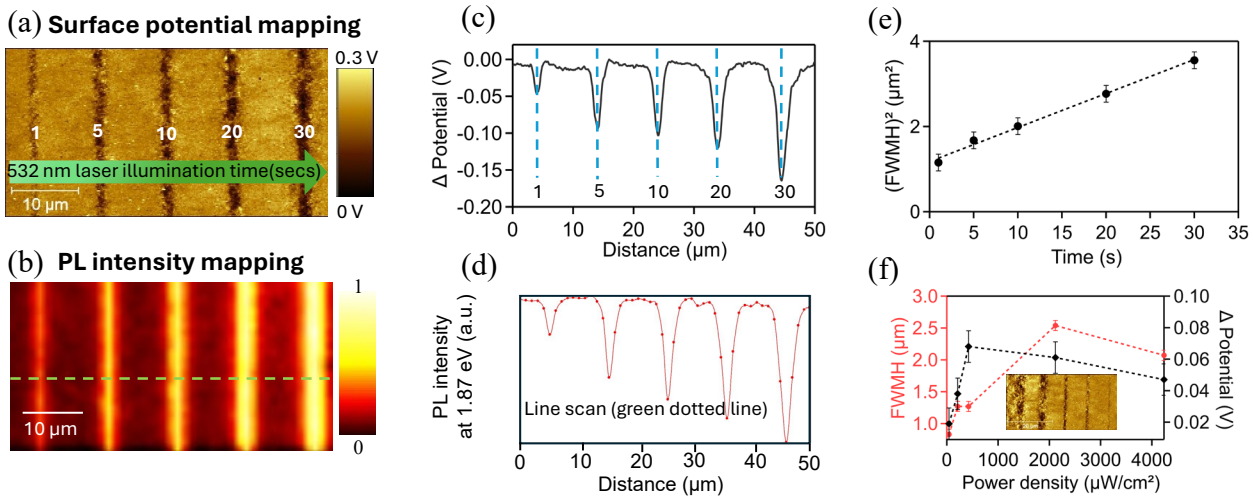

Fig. 3: Influence of illumination conditions i.e. time and power on photodedoping process. (a-e) shows data for various laser exposure times ranging from 1 to 30 s where the laser power is 423.7 µW/µm^2. (f) shows data for different laser power densities. (a) KPFM data showing changes in potential as the illumination time is varied. The numbers in white represent illumination time in seconds. (b) Corresponding PL mapping data showing PL with increase in illumination time. The mapping data has been acquired at 1.87 eV and PL intensity has been normalized to the pixel with the highest intensity. (c) Average line scan for potential changes extracted from the KPFM data. The average is taken along the y-direction in panel (a). (d) Line scan of PL at 1.87 eV along the green dash line in panel (b). (e) Change in (FWHM)^2 for potential peaks signifying broading due to diffusion. (f) Influence of power density of illumination on photo-dedoping process.

Although the power density for all illumination times in Fig. 3a and 3b is identical, the area affected by illumination changes (Fig. 3e). The broadening at the same power densities for different illumination times implicates additional mechanism(s) beyond light scattering. This broadening could arise from excitons or free carriers diffusing out of the illuminated area, leading to changes in dedoping densities over larger areas compared to the laser beam (~1.5 µm) itself. As

soon as the immediate area in the laser spot has been dedoped, carriers and excitons could diffuse beyond the illuminated area as their lifetime in the illuminated area increases and so they progressively reach further. To confirm this, we fit the full width half maximum (FWHM), of each peak in the Δ Potential scan of Fig. 3c to the diffusion equation ($FWHM-FWHM(t=0) \propto (Dt)^{1/2}$) (Fig. 3e) and found good agreement. The FWHM at t=0 is 1.08 µm, in good agreement with the known beam size. The fitting results in a diffusion coefficient of 0.03 $\mu m^2/s$, which is about 5 orders of magnitude slower than expected from the electron diffusion coefficient (10 $cm^2V^{-1}s^{-1}$)[53]. Thus, the diffusion behavior is limited by the kinetics of the dedoping process and not carrier transport. Ultimately this means that the best possible lateral resolution of the dedoping process is limited by the beam profile. Fig. 3f shows the influence of laser power on the dedoping process. At low power intensity, the PL intensity/degree of dedoping scales linearly with illumination power. However, higher powers (2.1 $mW/\mu m^2$ and 4.2 $mW/\mu m^2$) result in sample degradation.

Stability and scalability of photo-dedoping

The stability of dopants under ambient conditions as well as processing conditions form an important metric for device integration and performance[13].

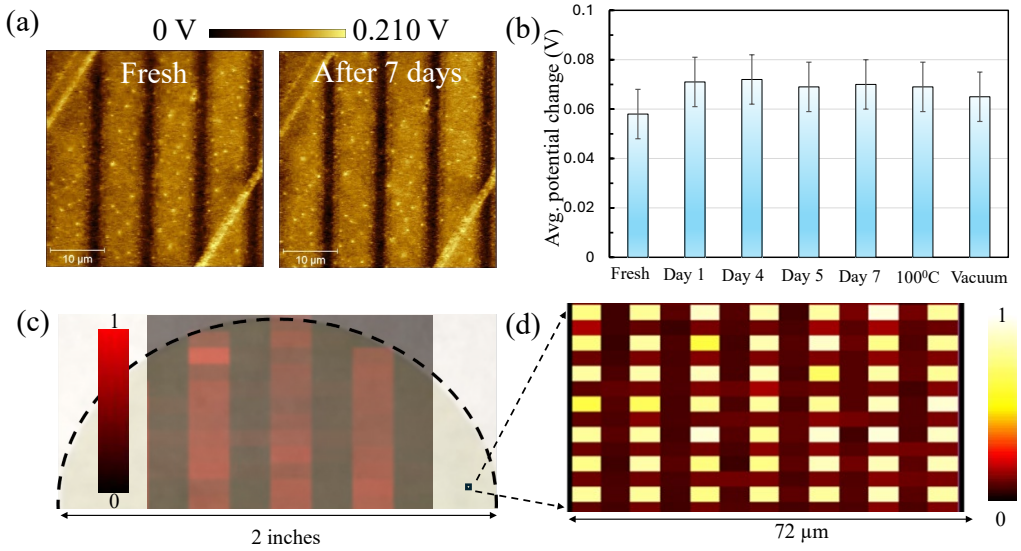

Fig. 4: Evaluating performance of the photode-doping process. (a) KPFM images comparing changes in photode-doping with high spatial resolution immediately after illumination and after 7 days post illumination. (b) Comparisons of change in potential (between the laser illuminated and not illuminated parts) over various stressing conditions like time, temperature and vacuum. (c) Photo-dedoping at wafer scale showing scalability of the process. PL intensity at 1.87 eV has been normalized to the pixel with the highest intensity. (d) Photo-dedoping at a much smaller length scale

showing control over spatial resolution of photo-dedoping with high spatial fidelity. PL intensity at 1.87 eV has been normalized to the pixel with the highest intensity.

Fig. 4a shows comparison for the surface potential maps a freshly photo-dedoped sample (few hours after exposure/illumination) and sample left in ambient conditions post photo-dedoping. It can be seen that there is hardly any change in the local doping densities of the samples for a period of 7 days signifying exceptional stability of the photo-dedoping procedure under ambient conditions.

KPFM images during intermediate periods (after 4 and 5 days) are shown in Fig. S8a and Fig. S8b. Importantly, the photo-dedoping in air effectively survives both heat (100 ^{o}C for 30 mins, Fig. S8c) and vacuum treatments (10 mTorr, Fig. S8d), demonstrating the resilience of the dedoping process to technologically relevant device processing conditions. Fig. 4b summarizes the average surface potential difference between the illuminated (dedoped) and not illuminated (as grown) parts as a function of these various processing conditions. We also tried testing the stability of the dedoping by PL measurements (Fig. S9), but the illumination with the laser excitation resulted in slight dedoping during the PL data acquisition, demonstrating the utility of KPFM for such stability measurements of photosensitive samples.

We also demonstrate the remarkable scalability and precision of photo-dedoping in MoS_2, enabling patterning over very large areas while maintaining fine spatial control. Specifically, we patterned across a 2-inch wafer (Fig. 4c) to showcase scalability. Simultaneously, we demonstrated significantly higher spatial fidelity on the same wafer (Fig. 4d), highlighting the precision of our technique. The high-spatial dedoping that can be achieved is constrained by the laser spot size and diffusion limits (1-2 μm) as discussed earlier.

Mechanism for photo-dedoping and impact on conductivity:

Two-terminal devices with channel widths of 10 μm were fabricated for electrical transport measurements (Fig. S10). The device fabrication process is discussed in detail in the material and methods section. Fig. 5a highlights the critical steps during the dedoping process which are elucidated by electrical measurements in Fig. 5b and Fig. 5c. Upon illumination, excitons are formed in MoS_2, which dissociate into electron hole pairs on the application of electrical bias between the source and the drain leading to an increase in channel conductance with a fast and slow component (Fig. 5b, green shaded region). The fast component is attributed to immediate

excess free carrier generation upon illumination, while the slow component is attributed to a photogating effect (Fig. 5a, part 1). The photogating effect has been observed in MoS_2 on amorphous oxide surfaces with oxygen vacancies, which act as trap sites for holes[54–56].

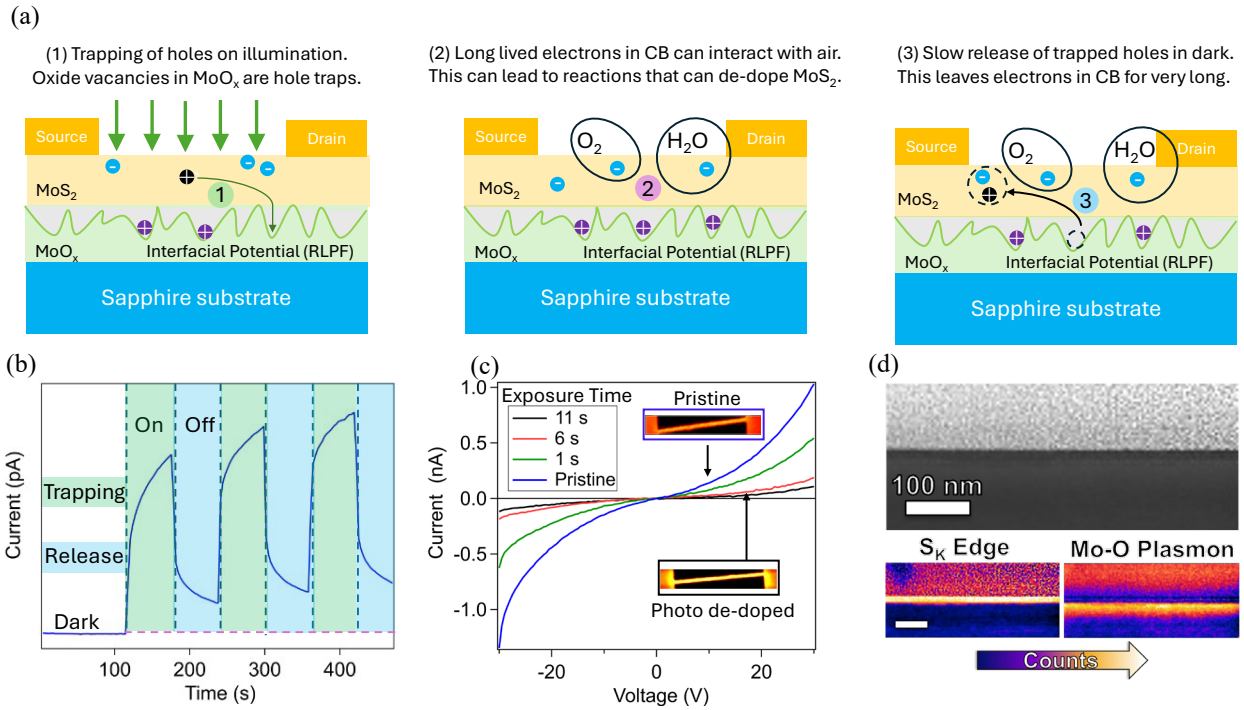

Fig. 5: Mechanism for photo-dedoping and change in channel conductance. (a) Mechanism for dedoping upon illumination. Step (i): The photoexcited holes get trapped in the MoO_x layer. This leads to a gradual increase in conductivity of the channel after the initial increase upon illumination due to photogating effect. Step (ii): The long-lived excited state electrons are energetic enough to participate in photoreactions in the presence ambient air. This leads to passivation of S vacancies on MoS_2. Concomitantly, this leads to the photo-dedoping effect. Step (iii): The holes are gradually released from the trapping layer when the light is turned off. This results in a slow decay in channel current after the initial decrease. (b) Transient measurements provide insights into the trapping/detrapping process upon illumination/dark. This compliments the mechanism for photo-dedoping in Fig. 5a. (c) I-V sweeps showing change in channel conductance post photo-dedoping. Inset shows the PL of the original sample and PL after 11 seconds illumination leading to photo-dedoping. The brighter regions (red/yellow) correspond to PL signal from MoS_2 and the darker (black) regions correspond to areas on the gold pad where there is no MoS_2 PL signal. Post dedoping the PL signal from the MoS_2 gets stronger. (d) STEM/EELS confirming the presence of the MoO_{3-x} layer. This oxide layer likely plays a critical role in trapping holes, enabling long-lived electrons in the conduction band in the dark.

To investigate the oxide layer, we used X-ray photoelectron spectroscopy (XPS), STEM-EELS, and Confocal Raman spectroscopy. The XPS data (Fig. S11) suggests the presence of MoO_3

like layer, while HAADF-STEM (top panel Fig. 5d) spatially resolves an oxide buffer layer between the MoS_2 and sapphire. The oxygen K-edge fine structure from STEM-EELS (bottom panel Fig. 5d) displayed a peak for the crystalline oxide in the substrate (~530 eV), which is not observed in the amorphous oxide layer directly underneath the deposited MoS_2 sample, indicating the oxide is amorphous (Fig. S12). Furthermore, the absence of signature MoO_3 Raman peaks confirms the amorphous nature. Together, the XPS, HAADF-STEM and Raman, we assign the oxide underneath the MoS_2 film as amorphous sub-stoichiometric MoO_{3-x}.

The MoO_{3-x} hole trapping layer plays a critical role in photo-dedoping MoS_2 in the presence of oxygen and moisture in ambient air. Hole trapping leads to the longer lifetime of electrons in the conduction band (CB) (during/post illumination). These electrons can participate in reactions with H_2O and O_2, likely leading to passivation of sulfur vacancies and dedoping of MoS_2 (Fig. 5a, part 2). We observe the long-lived electrons as a slow decrease in the measured MoS_2 photocurrent after stopping illumination, as the holes are slowly detrapped from the oxide layer and recombine with the electrons (Fig. 5a, part 3 and Fig. 5c, blue shaded region). While the photoconductivity decay is extremely slow (takes hours to reach steady state), the reaction of excited electrons with ambient air (O_2 and/or H_2O) dedoping the MoS_2 occurs at much shorter timescales as measured by PL and KFPM.

The long-lived electrons in the CB yield higher conductivity of the illuminated samples immediately after exposure leading to results that can be perceived as contradictory to our dedoping claims. Therefore, we measured the temporal dependence of current post-illumination) and found that it takes ~65 minutes for the dark current to fall below the dark current of the original (as grown) sample and even longer to reach steady state (~ 4-5 hours) (Fig. S13). We evaluated how photo-dedoping in MoS_2 measured with PL translated to changes in dark conductivity at steady state (measured after a day to ensure steady state, Fig. S14). As expected, different illumination times lead to different channel conductivities. We see almost an order of magnitude decrease with respect to as grown MoS_2 in steady-state dark current with an illumination time of 11 seconds (Fig. 5d). Corresponding PL images are shown in the inset and agree with our conclusions that the samples are dedoped with illumination. Our proposed mechanism highlight the critical roles of both ambient air and the oxide interface in the dedoping process.

As a final confirmation of the mechanism, we performed control PL experiments of MoS_2 monolayers (i) in an air-free cell (no moisture/O_2) and (ii) transferred to other substrates where the oxide interfacial layer is removed/changed due to transfer from growth substrate. Both these control experiments (Fig. S15 and Fig. S16) illustrate that the long-lived electrons can react with O_2/H_2O, provided these molecules are introduced before the carrier population reequilibrates to the ground state. This opens up unique possibilities for wafer scale, multi-logic devices with 2D atomically thin TMDCs for next generation electronic and optoelectronic devices.

Conclusions

In this work, we unravel the mechanism that drives PL changes of MoS_2 monolayers under laser illumination in ambient conditions. We demonstrate the critical role of the hole trap states within the oxide interface between the MoS_2 and the substrate for driving stable and long lived dedoping in wafer scale monolayer MoS_2. KPFM measurements confirm changes in fermi level position upon laser illumination leading to localized dedoping of monolayer MoS_2. We leverage this understanding to develop a scalable process with excellent spatial resolution to change doping densities in wafer scale monolayer MoS_2 by either controlling the illumination time or the power density. Further, time-lapsed KPFM measurements confirm that this dedoping is very stable under ambient conditions (at least 7 days) and survives high temperatures and vacuum conditions making it feasible for commercial deployment in semiconductor fabrication. We anticipate this ability to photo-dedope MoS_2 can be extended to other TMDCs where similar enhancements in PL upon illumination have been observed. This opens up unique possibilities for wafer scale, multi-logic devices with 2D atomically thin TMDCs for next generation electronic and optoelectronic devices.

Acknowledgements

This work was authored in part by the National Renewable Energy Laboratory, operated by Alliance for Sustainable Energy, LLC, for the U.S. Department of Energy (DOE) under Contract No. DE-AC36-08GO28308. Funding provided by Solar Photochemistry Program, Division of Chemical Sciences, Geosciences, and Biosciences, Office of Basic Energy Sciences, U.S. Department of Energy. The development and application of the modified probe station to allow in-situ device transport measurements of the photo-dedoping process was performed at the National Renewable Energy Laboratory and supported by the Reconfigurable Materials Inspired

by Nonlinear Neuron Dynamics (reMIND) Energy Frontier Research Center funded by the U.S. Department of Energy (DOE), Office of Science, Office of Basic Energy Sciences. C.S. received support from the U.S. DOE, Office of Science, Office of Workforce Development for Teachers and Scientists (WDTS) under the Science Undergraduate Laboratory Internships (SULI) Program. K.B. time was supported by the Virginia space grant consortium program under award number 005604. A portion of this research was conducted at the Center for Nanophase Materials Sciences, which is a DOE Office of Science User Facility.

Materials and Methods

Synthesis of large area monolayer MoS_2 films: MoS_2 is grown in a 3-zone tube furnace by Chemical Vapor Deposition (CVD). Solid phase precursors (MoO_3 and S) are loaded in separate heating zones of the CVD furnace and heated at different temperatures. The substrate (sapphire) is placed downstream in another zone which is maintained at a separate temperature. The schematic for the furnace and the temperature profiles are shown in Fig. S1. Argon is used as a carrier gas. The substrates are annealed before growth for high quality MoS_2 growth. During the anneal and growth, the pressure is maintained at 2 Torr. The substrates are annealed at 990 ^oC with flow rate of Ar maintained at 274 sccm and O_2 maintained at 5.56 sccm for 1.5 hours. The growth is started 25 minutes after the completion of annealing. The flow rate of Ar during the growth is maintained at 150 sccm. The substrates are placed in the heating zone of the furnace, which is maintained at 900 ^oC, the MoO_3 is maintained at 530 ^oC. The S is heated with an external heating belt maintained at 150 ^oC.

Photo-patterning procedure: We produced high spatial fidelity photo-patterns on MoS_2 by scanning the laser spot with local illumination at each one-micron spot for 30 seconds. This resulted in lines with illumination time of approximately 30 seconds. Multiple lines were created by rastering the laser. The spatial separation between 2 illuminated lines was maintained at 10 μm unless otherwise specified.

PL and Raman measurements: PL and Raman measurements were performed using the Renishaw inVia confocal system by using the 532 nm laser line and the 50× long working distance (50 mm) objective lens (spot size 1.5 μm diameter). The PL measurements were done at a laser

power of 1% (total power 75 μW) unless otherwise specified. The scattering light from the sample was directed by a grating with 1800 lines mm^{-1} for Raman or 600 lines mm^{-1} for PL prior to the CCD detector. The typical exposure time is 1 sec with two accumulations for PL measurements.

KPFM measurements:

Kelvin probe force microscopy (KPFM) is an extension of atomic force microscopy (AFM) technique. In KPFM, a conductive probe is used to record the surface potential of the sample, which is related to the work function of the sample surface. For semiconductors, the work function is defined as the energy difference between the Fermi energy level and the vacuum level. Thus, the surface potential obtained through KPFM is also related to the Fermi energy of the sample surface. Here, we obtained the surface potential images of the samples using our homemade KPFM with ~30 nm spatial and ~10 mV voltage resolutions. A Pt/Ir-coated conductive silicon AFM probe (Nanosensor PPP-EFM) with a tip apex radius of < 25 nm was used. For KPFM surface potential imaging, the second harmonic resonant oscillation frequency of the probe cantilever at 300–400 kHz was used, whereas the first harmonic resonance frequency at ~60 kHz was utilized for AFM topography imaging. A gold contact was deposited on the sample to ground the sample during KPFM measurement. The measured surface potential (also known as contact potential difference, V_{CPD}) is defined as

$$V_{CPD} = (\Phi_{tip} - \Phi_{sample})/e$$

Where Φ_{sample} and Φ_{tip} are work functions of the sample and the tip and, respectively. Freshly exfoliated highly oriented pyrolytic graphite (HOPG) having a known work function of 4.60 eV was used as a reference to estimate the work function of the tip (Fig. S17). The measured V_{CPD} between tip and HOPG was 0.60 ± 0.01 eV, from which we estimated that Φ_{tip} was 5.10 ± 0.01 eV. This work function value of the probe is used to obtain the change in work function of the monolayer MoS_2 upon illumination.

Device fabrication: Source (S) and Drain (D) pads were laid on the monolayer MoS_2 by standard photo lithography and metallization technique in the clean room. Initially S1818 positive photo resist (PR) was spin coated on top of Substrate/MoS_2 at 4000 RPM for 30 s followed by baking at 100 0C on the hot plate. The photoresist coated substrates were exposed to UV light of wavelength λ = 386 nm for 5.2 s through the photomask with the help of mask aligner. This was followed by

developing the PR in MF351: DI = 1:5 developer for 60 s and rinsing in DI water. Finally, to complete the device fabrication process, metallization process using e-beam evaporator was employed. Ti/Au = 5/50 nm was deposited at 10^{-6} Torr. Lift-off procedure was performed in acetone for 15 min followed by rinsing in IPA and drying in N_2 to attain S and D terminals. The quality of developing and liftoff was confirmed by microscope.

Transport measurements: Two-terminal current-voltage (I-V) characteristics of a planar MoS_2 device were carried out between source and drain terminal by utilizing the SMU unit of Keithley 4200-SCS parameter analyzer. All the electrical measurements were conducted inside the probe station in dark (unless otherwise specified), ambient atmosphere and pressure unless specified. Electrical contacts with the source and drain pads were done using spring-loaded micromanipulators with the aid of an optical microscope. To deplete the photo soaking effect in the devices caused by focusing the light from the microscope while probing the electrical contacts, the devices were allowed to rest for at least one hour before recording the actual I-V. After sufficient resting period, I-V curves were recorded by sweeping the voltage form -30 V to 30 V in step of 0.5 V and the corresponding current was collected. The transient data (current as a function of time) were recorded by biasing the voltage at 20 V.

TEM measurements: All TEM data was acquired using a Nion UltraSTEM 100 equipped with a Dectris ELA direct electron detector. The accelerating voltage of the electrons were set to 60 kV, a convergence semiangle of 30 mrad, and an EELS collection semi-angle of ~48 mrad. A 2mm EELS aperture was used to maximize the signal from the core-loss spectrum images.

XPS measurements: XPS data were obtained on a Physical Electronics Versa Probe III using Al Kα radiation. The XPS setup was calibrated with Au and/or Cu metal, which was cleaned via Ar-ion sputtering. The raw atomic concentration has a 5% error due to small signal to noise ratios of the monolayer and literature sensitivity values for peak integration. For these MoS_2 measurements on sapphire, we used the neutralizer (Ar ions and electrons) to compensate for charging effect.

Author Contributions:

D.G., N.H., L.H. and C.S. worked on CVD growth of MoS_2. D.G., N.H., L.H. and C.S carried out PL and Raman measurements. G.P. worked on KPFM measurements. E.M. performed XPS measurements. K.B. and J.A.H. worked on the HAADF-STEM imaging and EELS measurements. S.S. worked on the device fabrication. J.T. did gold deposition for the KPFM measurements. D.G. and S.S worked on the transport measurements. All authors helped to analyze and interpret the data. D.G., E.M., J.L., J.B. and A.F. wrote the paper. The project was directed and supervised by J.L. and E.M.

References

1. Splendiani, A. *et al.* Emerging Photoluminescence in Monolayer MoS_2. *Nano Lett.* **10**, 1271–1275 (2010).
2. Mak, K. F., Lee, C., Hone, J., Shan, J. & Heinz, T. F. Atomically Thin MoS_2 : A New Direct-Gap Semiconductor. *Phys. Rev. Lett.* **105**, 136805 (2010).
3. Sangwan, V. K. & Hersam, M. C. Neuromorphic nanoelectronic materials. *Nat. Nanotechnol.* **15**, 517–528 (2020).
4. Li, N. *et al.* Large-scale flexible and transparent electronics based on monolayer molybdenum disulfide field-effect transistors. *Nat Electron* **3**, 711–717 (2020).
5. Li, T. *et al.* Epitaxial growth of wafer-scale molybdenum disulfide semiconductor single crystals on sapphire. *Nat. Nanotechnol.* **16**, 1201–1207 (2021).
6. Xia, Y. *et al.* 12-inch growth of uniform MoS_2 monolayer for integrated circuit manufacture. *Nat. Mater.* **22**, 1324–1331 (2023).
7. Li, L. *et al.* Epitaxy of wafer-scale single-crystal MoS_2 monolayer via buffer layer control. *Nat Commun* **15**, 1825 (2024).
8. Chubarov, M. *et al.* Wafer-Scale Epitaxial Growth of Unidirectional WS_2 Monolayers on Sapphire. *ACS Nano* **15**, 2532–2541 (2021).

9. Kwon, J. *et al.* 200-mm-wafer-scale integration of polycrystalline molybdenum disulfide transistors. *Nat Electron* (2024) doi:10.1038/s41928-024-01158-4.

10. Fu, J.-H. *et al.* Oriented lateral growth of two-dimensional materials on c-plane sapphire. *Nat. Nanotechnol.* **18**, 1289–1294 (2023).

11. Das, S. *et al.* Transistors based on two-dimensional materials for future integrated circuits. *Nat Electron* **4**, 786–799 (2021).

12. Fan, D. *et al.* Two-dimensional semiconductor integrated circuits operating at gigahertz frequencies. *Nat Electron* **6**, 879–887 (2023).

13. Kim, J. *et al.* Area-Selective Chemical Doping on Solution-Processed MoS_2 Thin-Film for Multi-Valued Logic Gates. *Nano Lett.* **22**, 570–577 (2022).

14. Younas, R., Zhou, G. & Hinkle, C. L. A perspective on the doping of transition metal dichalcogenides for ultra-scaled transistors: Challenges and opportunities. *Applied Physics Letters* **122**, 160504 (2023).

15. Pham, V. P. & Yeom, G. Y. Recent Advances in Doping of Molybdenum Disulfide: Industrial Applications and Future Prospects. *Advanced Materials* **28**, 9024–9059 (2016).

16. Liu, W. *et al.* Light-induced activation of boron doping in hydrogenated amorphous silicon for over 25% efficiency silicon solar cells. *Nat Energy* **7**, 427–437 (2022).

17. Doping in 2D. *Nat Electron* **4**, 699–699 (2021).

18. Li, Z. *et al.* Revealing the biexciton and trion-exciton complexes in BN encapsulated WSe_2. *Nat Commun* **9**, 3719 (2018).

19. Liu, C. *et al.* Small footprint transistor architecture for photoswitching logic and in situ memory. *Nat. Nanotechnol.* **14**, 662–667 (2019).

20. Zhao, Z., Rakheja, S. & Zhu, W. Nonvolatile Reconfigurable 2D Schottky Barrier Transistors. *Nano Lett.* **21**, 9318–9324 (2021).

21. Ju, L. *et al.* Photoinduced doping in heterostructures of graphene and boron nitride. *Nature Nanotech* **9**, 348–352 (2014).

22. Choi, M. S. *et al.* High carrier mobility in graphene doped using a monolayer of tungsten oxyselenide. *Nat Electron* **4**, 731–739 (2021).

23. Yang, F.-S. *et al.* Oxidation-boosted charge trapping in ultra-sensitive van der Waals materials for artificial synaptic features. *Nat Commun* **11**, 2972 (2020).

24. Seo, S.-Y. *et al.* Reconfigurable photo-induced doping of two-dimensional van der Waals semiconductors using different photon energies. *Nat Electron* **4**, 38–44 (2020).

25. Wu, E. *et al.* Dynamically controllable polarity modulation of $MoTe_2$ field-effect transistors through ultraviolet light and electrostatic activation. *Sci. Adv.* **5**, eaav3430 (2019).

26. Peng, R. *et al.* Programmable graded doping for reconfigurable molybdenum ditelluride devices. *Nat Electron* **6**, 852–861 (2023).

27. Kim, H., Lien, D.-H., Amani, M., Ager, J. W. & Javey, A. Highly Stable Near-Unity Photoluminescence Yield in Monolayer MoS_2 by Fluoropolymer Encapsulation and Superacid Treatment. *ACS Nano* **11**, 5179–5185 (2017).

28. Shi, W. *et al.* Reversible writing of high-mobility and high-carrier-density doping patterns in two-dimensional van der Waals heterostructures. *Nat Electron* **3**, 99–105 (2020).

29. Lee, S.-J., Lin, Z., Duan, X. & Huang, Y. Doping on demand in 2D devices. *Nat Electron* **3**, 77–78 (2020).

30. Li, M. *et al.* P-type Doping in Large-Area Monolayer MoS_2 by Chemical Vapor Deposition. *ACS Appl. Mater. Interfaces* **12**, 6276–6282 (2020).

31. Ghoshal, D., Kumar, R. & Koratkar, N. Controlled Re doping in MoS_2 by chemical vapor deposition. *Inorganic Chemistry Communications* **123**, 108329 (2021).

32. Gao, J. *et al.* Transition-Metal Substitution Doping in Synthetic Atomically Thin Semiconductors. *Advanced Materials* **28**, 9735–9743 (2016).

33. Lee, S. Y. *et al.* Large Work Function Modulation of Monolayer MoS_2 by Ambient Gases. *ACS Nano* **10**, 6100–6107 (2016).

34. Ahn, J.-H., Parkin, W. M., Naylor, C. H., Johnson, A. T. C. & Drndić, M. Ambient effects on electrical characteristics of CVD-grown monolayer MoS_2 field-effect transistors. *Sci Rep* **7**, 4075 (2017).

35. Kim, E. *et al.* Site Selective Doping of Ultrathin Metal Dichalcogenides by Laser-Assisted Reaction. *Advanced Materials* **28**, 341–346 (2016).

36. Ly, T. H., Deng, Q., Doan, M. H., Li, L.-J. & Zhao, J. Facile Doping in Two-Dimensional Transition-Metal Dichalcogenides by UV Light. *ACS Appl. Mater. Interfaces* **10**, 29893–29901 (2018).

37. Afaneh, T., Sahoo, P. K., Nobrega, I. A. P., Xin, Y. & Gutiérrez, H. R. Laser-Assisted Chemical Modification of Monolayer Transition Metal Dichalcogenides. *Adv Funct Materials* **28**, 1802949 (2018).

38. Akkanen, S. M., Fernandez, H. A. & Sun, Z. Optical Modification of 2D Materials: Methods and Applications. *Advanced Materials* **34**, 2110152 (2022).

39. Hou, C. *et al.* Photoluminescence of monolayer MoS_2 modulated by water/O_2/laser irradiation. *Phys. Chem. Chem. Phys.* **23**, 24579–24588 (2021).

40. Ardekani, H., Younts, R., Yu, Y., Cao, L. & Gundogdu, K. Reversible Photoluminescence Tuning by Defect Passivation via Laser Irradiation on Aged Monolayer MoS_2. *ACS Appl. Mater. Interfaces* **11**, 38240–38246 (2019).

41. Rao, R. *et al.* Dynamics of cleaning, passivating and doping monolayer MoS_2 by controlled laser irradiation. *2D Mater.* **6**, 045031 (2019).

42. Sivaram, S. V. *et al.* Spatially Selective Enhancement of Photoluminescence in MoS_2 by Exciton-Mediated Adsorption and Defect Passivation. *ACS Appl. Mater. Interfaces* **11**, 16147–16155 (2019).

43. Atkin, P. *et al.* Laser exposure induced alteration of WS_2 monolayers in the presence of ambient moisture. *2D Mater.* **5**, 015013 (2017).

44. Kim, H.-J., Yun, Y. J., Yi, S. N., Chang, S. K. & Ha, D. H. Changes in the Photoluminescence of Monolayer and Bilayer Molybdenum Disulfide during Laser Irradiation. *ACS Omega* **5**, 7903–7909 (2020).

45. Lu, J. *et al.* Atomic Healing of Defects in Transition Metal Dichalcogenides. *Nano Lett.* **15**, 3524–3532 (2015).

46. Huang, X. *et al.* Neutralizing Defect States in MoS_2 Monolayers. *ACS Appl. Mater. Interfaces* **13**, 44686–44692 (2021).

47. Oh, H. M. *et al.* Photochemical Reaction in Monolayer MoS_2 *via* Correlated Photoluminescence, Raman Spectroscopy, and Atomic Force Microscopy. *ACS Nano* **10**, 5230–5236 (2016).

48. Zhang, H. *et al.* Disentangling oxygen and water vapor effects on optoelectronic properties of monolayer tungsten disulfide. *Nanoscale* **12**, 8344–8354 (2020).

49. Wang, L. *et al.* Laser Annealing Improves the Photoelectrochemical Activity of Ultrathin $MoSe_2$ Photoelectrodes. *ACS Appl. Mater. Interfaces* **11**, 19207–19217 (2019).

50. Qiu, H. *et al.* Hopping transport through defect-induced localized states in molybdenum disulphide. *Nat Commun* **4**, 2642 (2013).

51. Shen, P.-C. *et al.* Healing of donor defect states in monolayer molybdenum disulfide using oxygen-incorporated chemical vapour deposition. *Nat Electron* **5**, 28–36 (2021).

52. Kim, B.-K. *et al.* Origins of genuine Ohmic van der Waals contact between indium and MoS_2. *npj 2D Mater Appl* **5**, 9 (2021).

53. Radisavljevic, B. & Kis, A. Mobility engineering and a metal–insulator transition in monolayer MoS_2. *Nature Mater* **12**, 815–820 (2013).

54. Lopez-Sanchez, O., Lembke, D., Kayci, M., Radenovic, A. & Kis, A. Ultrasensitive photodetectors based on monolayer MoS_2. *Nature Nanotech* **8**, 497–501 (2013).

55. Wu, Y.-C. *et al.* Extrinsic Origin of Persistent Photoconductivity in Monolayer MoS_2 Field Effect Transistors. *Sci Rep* **5**, 11472 (2015).

56. Chen, P.-H. *et al.* Passivated Interfacial Traps of Monolayer MoS_2 with Bipolar Electrical Pulse. *ACS Appl. Mater. Interfaces* **15**, 10812–10819 (2023).